Bixbyite-type Ln_2O_3 as promoters of metallic Ni for alkaline electrocatalytic hydrogen evolution

Hongming Sun[1,4], Zhenhua Yan[2,4], Caiying Tian[1,4], Cha Li[1,4], Xin Feng[1], Rong Huang[1], Yinghui Lan[1], Jing Chen[1], Cheng-Peng Li [1✉], Zhihong Zhang [3] & Miao Du [1,3✉]

The active-site density, intrinsic activity, and durability of Ni-based catalysts are critical to their application in industrial alkaline water electrolysis. This work develops a kind of promoters, the bixbyite-type lanthanide metal sesquioxides (Ln_2O_3), which can be implanted into metallic Ni by selective high-temperature reduction to achieve highly efficient Ni/Ln_2O_3 hybrid electrocatalysts toward hydrogen evolution reaction. The screened Ni/Yb_2O_3 catalyst shows the low overpotential (20.0 mV at 10 mA cm^{-2}), low Tafel slope (44.6 mV dec^{-1}), and excellent long-term durability (360 h at 500 mA cm^{-2}), significantly outperforming the metallic Ni and benchmark Pt/C catalysts. The remarkable hydrogen evolution activity and stability of Ni/Yb_2O_3 are attributed to that the Yb_2O_3 promoter with high oxophilicity and thermodynamic stability can greatly enlarge the active-site density, reduce the energy barrier of water dissociation, optimize the free energy of hydrogen adsorption, and avoid the oxidation corrosion of Ni.

[1] College of Chemistry, Tianjin Key Laboratory of Structure and Performance for Functional Molecules, Tianjin Normal University, 300387 Tianjin, China. [2] Key Laboratory of Advanced Energy Materials Chemistry (Ministry of Education), College of Chemistry, Nankai University, 300071 Tianjin, China. [3] College of Materials and Chemical Engineering, Zhengzhou University of Light Industry, 450001 Zhengzhou, China. [4] These authors contributed equally: Hongming Sun, Zhenhua Yan, Caiying Tian, Cha Li. ✉email: hxxylcp@tjnu.edu.cn; hxxydm@tjnu.edu.cn

Hydrogen (H_2) production via water electrolysis powered by solar or wind energy technologies is envisioned as an efficient strategy to meet the rising demands for renewable and clean energy resources[1,2]. As few non-noble electrocatalysts show adequate oxygen evolution reaction (OER) performance under acidic conditions, tremendous efforts have been devoted to develop the low-cost, robust and high-efficiency electrocatalysts for hydrogen evolution reaction (HER) that can be compatible with the alkaline media[3,4]. Particularly, metallic Ni with low price, high electrical conductivity, and promising alkaline HER activity has been extensively explored as the cathode material for industrial water electrolysis almost a century ago[4–7]. Nevertheless, the alkaline HER electrocatalytic activity of metallic Ni is still far from satisfactory owing to its strong hydrogen adsorption and the lack of effective water dissociation sites for sluggish Volmer step of alkaline HER[4–7]. Moreover, metallic Ni catalyst is often subjected to serious deactivation for prolonged water electrolysis, owing to the chemical corrosion by oxygen diffusion and/or strong hydrogen adsorption[8–10]. Hence, designing and exploiting efficient and durable metallic Ni-based alkaline HER catalysts, which can meet the requirement of commercial electrolyzers, is highly appealing yet challenging.

Inducing the oxophilic species into HER electrocatalysts is a valid strategy to improve their alkaline catalytic activities, which will favor the cleaving of H–OH bonds in H_2O molecule and thereby facilitate the sluggish Volmer step of alkaline HER[11–13]. The transition-metal oxides and hydroxides have been widely used as the foreign oxophilic compounds, which can couple with HER catalysts to afford highly active hybrids such as $Pt/Ni(OH)_2$, $Ni/Ni(OH)_2$, $Pt/(Fe,Ni)(OH)_2$, $Co(OH)_2/MoS_2$, Ni/NiO, $Ru/(Fe,Ni)(OH)_2$, etc.[9,14–18]. Nevertheless, their stability at high current density is still inferior owing to the low thermodynamic stability of these oxides and hydroxides, which readily convert to metals or low-valence species under the highly reductive potential[8,19,20]. Alternatively, lanthanide oxides with high thermodynamic stability and oxophilicity are a class of promising promoters toward water dissolution. In this context, fluorite-type ceria (CeO_2) has shined in a variety of catalytic fields[21,22], for which the easy conversion between Ce^{3+} and Ce^{4+} endows it with excellent redox capability. Moreover, the specific crystal structure and reversible valence of CeO_2 enable the formation of oxygen vacancy. These unique properties such as high oxophilicity, multivalence, and rich oxygen vacancies ensure the formation of strong interaction between CeO_2 and the active component to enhance the catalytic performances[22,23]. As a result, CeO_2 has been extensively applied as the "performance promoter" of numerous electrocatalysts for different reactions, such as HER, hydrogen oxidation reaction (HOR), OER, oxygen reduction reaction (ORR), methanol oxidation reaction (MOR), CO_2 reduction reaction (CO_2RR), and nitrogen reduction reaction (NRR), etc[24–30]. For example, doping CeO_2 with Ni, Co, Ni_2P, Co_4N, CoP or NiCo etc could remarkably enhance the HER catalytic activity in alkaline media[24,31–34]. Nevertheless, their HER performances are still not comparable to the Pt-based electrocatalysts. One possible reason is the unmanageable balance between the H-/OH-binding energy and H_2O-dissociation energy of the catalysts. Notably, the different degrees of oxophilicity for lanthanide metal oxides provide the opportunities to screen new water-dissociation promoters with a better matching to metallic Ni, which thus may concurrently realize the low water-dissociation energy barrier and the optimized H-/OH-binding energies. In this context, the bixbyite-type lanthanide sesquioxides (Ln_2O_3, Ln = Sm, Eu, Gd, Dy, Ho, Er, Tm, Yb, and Lu) are often described as the fluorite-type CeO_2 structure with ordered oxygen vacancies[35], thereby showing potential as the performance promoters for alkaline HER, which however are unexplored thus far.

In this work, we prepare a series of graphite plate (GP) supported Ni/Ln_2O_3 hybrids by the selective high-temperature reduction approach. Remarkably, the Ni/Ln_2O_3 electrodes illustrate higher HER activity and long-term stability relative to the Ni electrode, and the enhancement effect of Ln_2O_3 as excellent electrocatalytic promoters is revealed. Furthermore, the screened Ni/Yb_2O_3 hybrid, with both the low H_2O-dissociation energy barrier and the optimized H-/OH-binding energy, exhibits significantly higher electrocatalytic HER activity than the well-known Ni/CeO_2, revealing that Yb_2O_3 is a preferable promoter than CeO_2 for HER in alkaline condition. Additionally, the strong coupled Yb_2O_3 with high thermodynamic stability not only prevents the agglomerate of Ni during high-temperature sintering, but also avoids the chemical corrosion of Ni during the long-term HER tests. The current finding not only opens up the applications of cubic bixbyite-type Ln_2O_3 as electrocatalytic promotors, but also makes Ni/Yb_2O_3 a promising cathode material for commercial electrolyzers.

Results

Preparation and characterizations of the Ni/Ln_2O_3 electrodes. A selective high-temperature reduction method was developed to synthesize the Ni/Ln_2O_3 electrodes (see Fig. 1a). First, the $Ni(OH)_2/Ln(OH)_3$ precursor was loaded on a graphitic substrate (Supplementary Fig. 1) by a simple NO_3^- reduction electrodeposition method[36]. In the electrodeposition process, NO_3^- is reduced and the produced OH^- leads to the synchronous generation of $Ni(OH)_2$ and $Ln(OH)_3$[34]. The ultralow solubility of $Ni(OH)_2$ and $Ln(OH)_3$ ensures their rapid and quantitative deposition on the graphitic substrate with excellent chemical homogeneity. Taking Ni/Yb_2O_3 as an example, after deposition of the $Ni(OH)_2/Yb(OH)_3$ precursor, the gray graphitic substrate turns green (Supplementary Figs. 2–4). During the following high temperature sintering, $Yb(OH)_3$ will decompose into Yb_2O_3 below 500 °C (Supplementary Fig. 5). From the viewpoint of thermodynamics ($\triangle_r G_m^\theta = \triangle_r H_m^\theta - T\triangle_r S_m^\theta$), a high temperature beyond ca. 10,000 °C is required to reduce Yb_2O_3 to Yb under H_2 atmosphere, whereas $Ni(OH)_2$ could be reduced to metallic Ni by H_2 at 0 °C (Supplementary Table 1). Therefore, the $Ni(OH)_2/Yb(OH)_3$ precursor can be selectively converted to Ni/Yb_2O_3 at 500 °C under a H_2/Ar (10%) atmosphere. Due to the similarity of thermodynamic parameters for Ln_2O_3, homologous Ni/Ln_2O_3 could be obtained by this method as well. Moreover, this selective high-temperature reduction method is available to prepare various metal/metal oxide hybrids.

The X-ray diffraction (XRD) patterns (Fig. 1b) of Ni/Ln_2O_3 nanoparticles scraped off the graphite plate are similar. The peaks at 28.3–29.6°, 32.6–34.4°, 47.2–49.4°, and 56.0–58.7° are attributed to the (222), (400), (440), and (622) facets of the cubic bixbyite-type Ln_2O_3. Figure 1c presents the bixbyite structure of Ln_2O_3 with a face-centered cubic (fcc) unit cell of Ln centers, which are coordinated by six nearest-neighboring oxygen atoms. The bixbyite-type Ln_2O_3, also known as the C-type rare-earth oxide structure according to the Goldschmidt's classification, is generally considered as the defect cubic fluorite-type CeO_2 with ordered oxygen vacancies (Fig. 1d)[35]. Moreover, the other diffraction peaks (Fig. 1b) at 44.5°, 51.8°, and 76.4°, respectively, are assigned to the (111), (200), and (220) facets of cubic Ni (JCPDS No. 4-850, space group $Pm3m$, Supplementary Fig. 6), which reveals the formation of Ni/Ln_2O_3 hybrids. The scanning electron microscopy (SEM) images of Ni/Ln_2O_3 electrodes indicate that the Ni/Ln_2O_3 nanoparticles uniformly cover over the graphitic plate (Supplementary Figs. 7–15). The Ni/Ln atomic ratios obtained from energy-dispersive spectroscopy (EDS) analysis, are all ca. 90/10 in these Ni/Ln_2O_3 hybrids, which are similar to the initial Ni^{2+}/Ln^{3+}
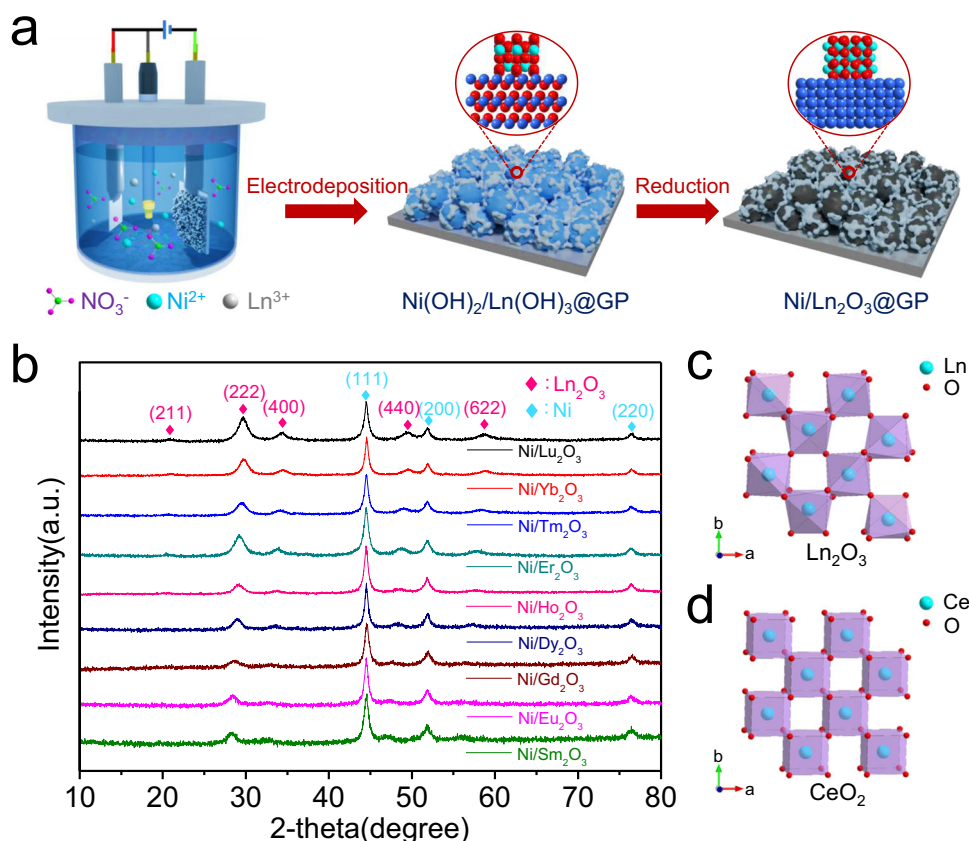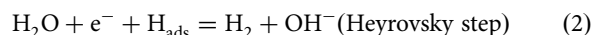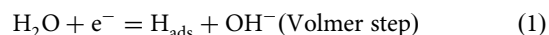
Fig. 1 Preparation and phase analysis of electrodes. a Synthetic scheme of graphite plate supported Ni/Ln_2O_3 electrodes. **b** XRD patterns of Ni/Ln_2O_3 hybrids. **c** Crystal structure of bixbyite-type Ln_2O_3. **d** Crystal structure of fluorite-type CeO_2.

feed ratio. X-ray photoelectron spectroscopy (XPS) tests of Ni/Ln_2O_3 indicate that Ni is metallic state and the Ln elements are trivalent (Supplementary Figs. 7–15). The above results confirm the successful preparation of a series of Ni/Ln_2O_3 electrodes with analogous chemical compositions, morphologies and crystal structures, thus resulting in the comparability of their HER catalytic activities. For a comparison, the pristine Ni nanoparticles on graphite plate (Ni electrode, Supplementary Fig. 16) and Ln_2O_3 nanoparticles on graphite plates (Ln_2O_3 electrodes, Supplementary Figs. 17 and 18) were prepared by the similar procedure.

Electrocatalytic HER activities of the Ni/Ln_2O_3 electrodes. The HER catalytic performances of Ln_2O_3 (Sm_2O_3, Eu_2O_3, Gd_2O_3, Dy_2O_3, Ho_2O_3, Er_2O_3, Tm_2O_3, Yb_2O_3, and Lu_2O_3) electrodes were tested in 1.0 M KOH (Supplementary Fig. 19). The Ln_2O_3 electrodes show negligible HER catalytic activity with high overpotentials. The linear sweep voltammetry (LSV) polarization curves (Fig. 2a) reveal that the Ni/Ln_2O_3 electrodes with Ln_2O_3 coupling show remarkably improved electrocatalytic activity than the pristine Ni electrode. Interestingly, to drive a current density of 100 mA cm^{-2}, the overpotentials of Ni/Ln_2O_3 electrodes decrease in turn from Ni/Sm_2O_3 (184.3 mV) to Ni/Yb_2O_3 (81.0 mV), and ultimately, slightly increase to 84.0 mV for Ni/Lu_2O_3. Remarkably, the overpotentials of Ni/Ln_2O_3 electrodes (81.0–184.3 mV) are all lower than that of Ni electrode (217.1 mV).

The Tafel slopes of electrodes were applied to judge the reaction mechanism (Fig. 2b). The lowest Tafel slope is found for Ni/Yb_2O_3 (44.6 mV dec^{-1}) and the highest Tafel slope is observed for Ni/Sm_2O_3 (116.7 mV dec^{-1}). Similarly, the Tafel slopes for Ni/Ln_2O_3 electrodes are all lower than that for Ni

electrode (124.9 mV dec^{-1}). The Tafel values of Ni/Ln_2O_3 electrodes reveal that the HER follows the Volmer–Heyrovsky mechanism[37,38]:

$$H_2O + e^- = H_{ads} + OH^- (\text{Volmer step}) \qquad (1)$$

$$H_2O + e^- + H_{ads} = H_2 + OH^- (\text{Heyrovsky step}) \qquad (2)$$

The high Tafel slope of Ni electrode reveals that the Volmer step is the rate-determining step[39,40]. That is, the Ln_2O_3 coupling will greatly facilitate the sluggish water dissociation process of HER on metallic Ni, and the facilitating effect increases from Sm_2O_3 to Yb_2O_3 and Lu_2O_3. A comparison of the Tafel slope and the overpotential at 100 mA cm^{-2} evidently demonstrates that the Ni/Ln_2O_3 electrodes outperform the Ni electrode, and Ni/Yb_2O_3 has the highest catalytic activity among all Ni/Ln_2O_3 electrodes (Fig. 2c). The turnover frequencies (TOFs) of Ni/Ln_2O_3 and Ni electrodes were further calculated to reveal their intrinsic activities. The corresponding active sites of electrodes were quantified using electrochemical active surface areas (ECSAs) (Supplementary Figs. 20 and 21). The Ni/Ln_2O_3 electrodes perform the larger ECSAs and thus have more active sites than Ni electrode. Remarkably, the Ni/Ln_2O_3 electrodes still show higher TOF than Ni electrode after averaging over each of the active sites (Fig. 2d). Specifically, at an overpotential of 100 mV, Ni/Sm_2O_3 shows the smallest TOF (0.026 H$_2$ s^{-1}) and Ni/Yb_2O_3 shows the largest TOF (0.362 H$_2$ s^{-1}), which is 15 times higher than that of Ni electrode (0.024 H$_2$ s^{-1}), indicating that the Ni/Yb_2O_3 electrode has greatly enhanced intrinsic HER activity in alkaline media compared with the Ni electrode (Supplementary Fig. 22).

To understand the origin of electrocatalytic activity and the role of Ln_2O_3, electrochemical impedance spectroscopy (EIS) was
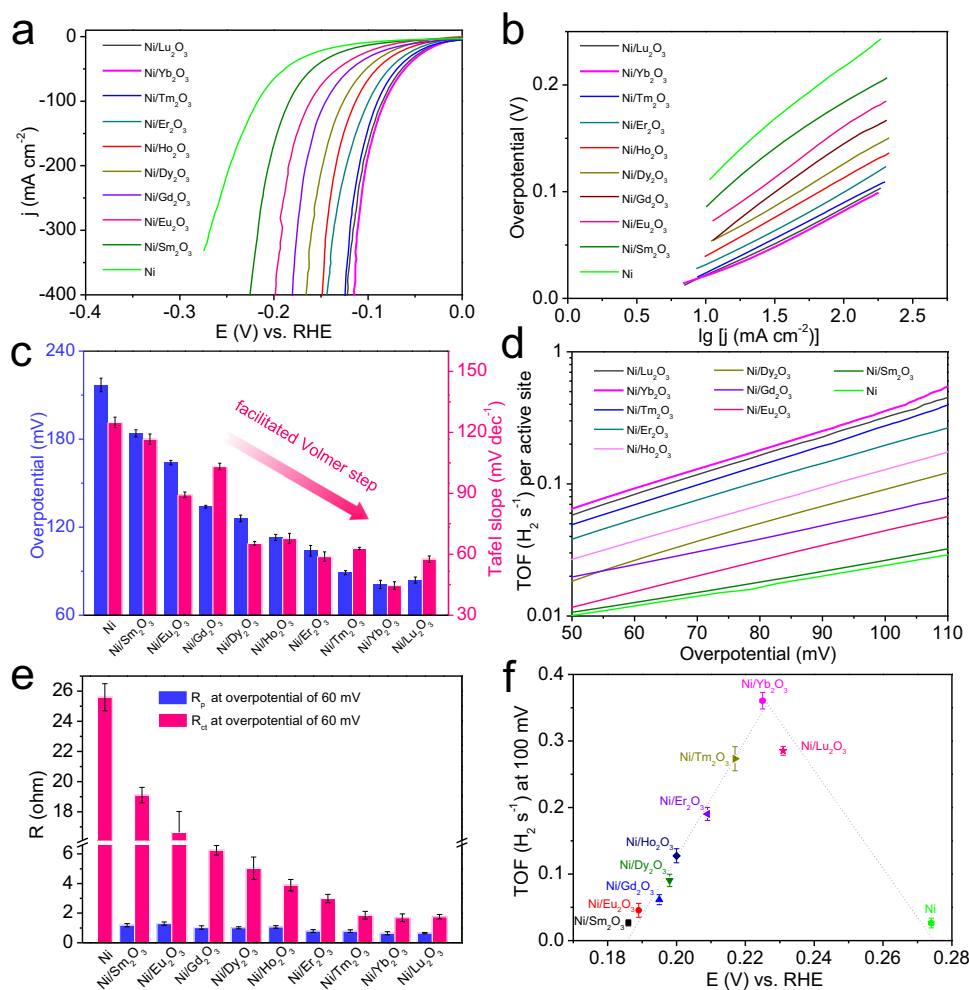
Fig. 2 Electrocatalytic HER activity of the Ni/Ln$_2$O$_3$ electrodes in 1.0 M KOH electrolyte. a Polarization curves (scan rate: 5 mV s^{-1}) of the Ni/Ln$_2$O$_3$ and Ni electrodes with mass loading of ca. 3.5 mg cm^{-2}. **b** The corresponding Tafel plots. **c** Comparison of catalytic activity in term of the overpotential at 100 mA cm^{-2} and Tafel slopes. **d** TOF values of the Ni/Ln$_2$O$_3$ and Ni electrodes. **e** Comparison of the charge transfer resistance (R_{ct}) and mass transfer resistance (R_p) of the Ni/Ln$_2$O$_3$ and Ni electrodes. **f** Volcano plot of TOF value at 100 mV as a function of potential for the OH adsorption peak of the Ni/Ln$_2$O$_3$ and Ni electrodes. The error bars in **c**, **e**, and **f** show the standard derivation based on triplicate measurements.

tested at different overpotentials (Supplementary Figs. 23 and 24a) for Ni/Ln$_2$O$_3$ and Ni electrodes. The Randles electrical equivalent circuit model is used to interpret the AC impedance of HER on Ni electrode without a response related to the hydrogen adsorption, and the Armstrong equivalent circuit is used to explain the AC impedance behavior on Ni/Ln$_2$O$_3$ electrodes as the second semicircle in Nyquist curves (Supplementary Fig. 24b)[41]. In Armstrong equivalent circuit model, R_{ct} reveals the charge transfer resistance (low frequency semicircle) for electrode reaction, and R_p indicates the mass transfer resistance (high frequency semicircle) of adsorbed intermediate H_{ads}[42]. The EIS spectra of Ni/Ln$_2$O$_3$ and Ni electrodes both exhibit the expected behaviors when increasing the overpotentials, that is, the total resistances decrease with the increase of overpotentials (Supplementary Figs. 23 and 24a). The main difference is found for the R_{ct} values of Ni/Ln$_2$O$_3$ electrodes, which decrease from Ni/Sm$_2$O$_3$ to Ni/Yb$_2$O$_3$ and then, slightly increase for Ni/Lu$_2$O$_3$. Also, all R_{ct} values of Ni/Ln$_2$O$_3$ are lower than that of Ni at the overpotentials from 20 to 100 mV (Fig. 2e, Supplementary Fig. 24c and supplementary Table 2). As the rate-determining step of alkaline HER is the Volmer reaction, the R_{ct} of Ni electrode should mainly arise from the sluggish Volmer reaction[41]. Correlating the regular variations of catalytic activities with the consistent R_{ct} sequences for Ni/Ln$_2$O$_3$ and Ni electrodes,

we believe that the Ln$_2$O$_3$ promotor can activate water and facilitate the sluggish water decomposition step (Volmer step) of the alkaline HER on Ni, which agrees well with the results derived from the Tafel slopes. Moreover, the R_p values of Ni/Ln$_2$O$_3$ electrodes are small and not changed obviously, showing a slight decrease from Ni/Sm$_2$O$_3$ to Ni/Lu$_2$O$_3$, which indicates that the mass transfer behaviors of adsorbed intermediate (H_{ads}) are not dominating in regulating the catalytic activities of Ni/Ln$_2$O$_3$ electrodes.

It is known that the reaction barrier for water dissociation step of alkaline HER is governed by the adsorption energy of hydroxyl species (OH$_{ads}$)[6,43]. Herein, the incorporation of oxophilic Ln$_2$O$_3$ in Ni/Ln$_2$O$_3$ could strengthen the OH-binding energy, thereby accelerating the adsorption of water molecules and cleaving of HO–H bond[44]. To verify this inference, the cyclic voltammogram (CV) curves for OH adsorption and desorption on the surfaces of Ni/Ln$_2$O$_3$ and Ni electrodes were measured (Supplementary Fig. 25). For Ni/Ln$_2$O$_3$, an obvious negative shift of OH adsorption peak (ca. 0.186–0.231 V) compared with that of Ni (ca. 0.274 V) is observed, which shows the stronger OH-binding energy on surface of Ni/Ln$_2$O$_3$ electrodes than that of Ni electrode[45]. Moreover, the OH adsorption potentials for Ni/Ln$_2$O$_3$ electrodes gradually decrease with a variation of decorated

Ln_2O_3 from Sm_2O_3 to Lu_2O_3, which is consistent with the regular changes of oxophilicity for these Ln elements in the same period. More interestingly, a volcano relation could be achieved from the TOF values at 100 mV for Ni/Ln_2O_3 and Ni electrodes, as a function of experimentally measured OH adsorption potentials (Fig. 2f). The volcano relation reveals that there may exist an optimal value of OH-binding energy, which reflects the Sabatier principle that the optimized electrocatalysts would adsorb the intermediates neither too strongly nor too weakly[15,46]. The Ni and Ni/Lu_2O_3 electrodes have the relatively weaker OH adsorption, which cannot facilitate the water dissociation effectively. In contrast, the strong OH adsorption ability from Ni/Sm_2O_3 to Ni/Tm_2O_3 can promote the water adsorption and dissociation availably, which however may also impede the OH desorption and thus block the active sites. As a result, the Ni/Yb_2O_3 electrode with a proper OH binding ability can realize an optimal balance between promoting the H_2O dissociation and preventing the poisoning effect[43]. The regular changes of OH adsorption ability of Ni/Ln_2O_3 could also be confirmed by their O 1s XPS spectra collected under normal atmospheric pressure and 25 °C (Supplementary Fig. 26). The peaks of O 1s XPS spectra can be assigned to the absorbed OH groups and O atoms from Ln_2O_3 lattice. Obviously, the OH coverage gradually decreases from Ni/Sm_2O_3 to Ni/Lu_2O_3, which indicates the reduced adsorption strength of OH from Ni/Sm_2O_3 to Ni/Lu_2O_3[47,48].

Analysis of microstructures and chemical environments for Ni/Yb_2O_3. To obtain the deeper insights into the origin of excellent HER performances for Ni/Yb_2O_3, the contrast experiments and structural/component characterizations were carried out. Firstly, the Ni/Yb_2O_3 hybrids with diverse compositions (99:1, 97:3, 95:5, 90:10, 80:20, 70:30, and 60:40) were similarly prepared to confirm the optimal Ni:Yb molar ratio (Supplementary Fig. 27 and Supplementary Table 3). As observed in Supplementary Fig. 27, those Ni/Yb_2O_3—99:1, Ni/Yb_2O_3—97:3, Ni/Yb_2O_3—95:5, Ni/Yb_2O_3—80:20, Ni/Yb_2O_3—70:30, and Ni/Yb_2O_3—60:40 also show the similar morphology of nanoparticle arrays to that of Ni/Yb_2O_3—90:10 (i.e. Ni/Yb_2O_3—90:10). The XRD patterns (Fig. 3a) interestingly suggest that as the ratio of Yb_2O_3 increases, the (111) facet of cubic Ni gradually shifts to smaller diffraction angles for these Ni/Yb_2O_3 hybrids, which reveals the slight lattice expansion of Ni nanoparticles and the enhanced coupling between Ni and Yb_2O_3. Moreover, as the content of Yb_2O_3 increases, the crystallite size of Ni nanoparticles decreases and that of Yb_2O_3 increases gradually (Fig. 3b), as determined from the XRD peak widths of Ni(111) and Yb_2O_3(222) using the Debye–Scherrer equation. This reveals that the introduction of Yb_2O_3 can significantly lower the size of Ni phase, because Yb_2O_3 with high thermodynamic stability will prevent the agglomeration of Ni in the annealing process. The reduced sizes of Ni nanoparticles can enhance the active-site density in the Ni/Yb_2O_3 hybrids. As the content of Yb_2O_3 increases, the ECSAs of these Ni/Yb_2O_3 hybrids (Ni/Yb_2O_3—99:1, Ni/Yb_2O_3—97:3, Ni/Yb_2O_3—95:5 and Ni/Yb_2O_3—90:10) increases gradually. But when excessive Yb_2O_3 is doped, the ECSAs of the Ni/Yb_2O_3 hybrids will be decreased, because the smaller ECSA of Yb_2O_3 lowers the total ECSAs of the Ni/Yb_2O_3 hybrids (Supplementary Figs. 28 and 29). As a result, Ni/Yb_2O_3—90:10 with appropriate doping amount of Yb_2O_3 shows the highest ECSA among the Ni/Yb_2O_3 electrodes with different compositions (Supplementary Fig. 30). The result is also consistent with the higher Brunauer–Emmett–Teller (BET) specific surface area of Ni/Yb_2O_3 ($29.0\ m^2\ g^{-1}$) compared with that of Ni ($18.1\ m^2\ g^{-1}$), as evaluated by their N_2 sorption isotherms (Supplementary Fig. 31).

The transmission electron microscopy (TEM) image (Supplementary Fig. 32a) shows that Ni/Yb_2O_3 consists of the closely interconnected nanoparticles. The TEM mapping confirms the homogenous distribution of Ni, Yb and O elements (Fig. 3c). High-resolution TEM (HRTEM) image of Ni/Yb_2O_3 (Fig. 3d) indicates well-resolved lattice fringes with the interplanar spacing of 0.204 and 0.301 nm calculated from non-interface area, which could be assigned to Ni(111) and Yb_2O_3(222), respectively. The HRTEM images (Fig. 3d, Supplementary Fig. 32b, c) show that each Ni nanoparticle is surrounded by some Yb_2O_3 nanocrystallines. As indicated by TEM mapping and HRTEM images (Supplementary Figs. 33–38) of the other Ni/Yb_2O_3 hybrids with different Ni:Yb molar ratios (Ni/Yb_2O_3—99:1, Ni/Yb_2O_3—97:3, Ni/Yb_2O_3—95:5, Ni/Yb_2O_3—80:20, Ni/Yb_2O_3—70:30, and Ni/Yb_2O_3—60:40), the Ni and Yb_2O_3 nanoparticles are also mixed in form of heterojunction structures, and the Yb_2O_3 nanocrystallines are distributed on the surface of Ni nanoparticles. Furthermore, as the content of Yb increases, the number of Yb_2O_3 nanoparticles increases and the size of Ni nanoparticles decreases clearly, which is consistent with the results of particle size analysis from the XRD patterns.

In other TEM images (Supplementary Fig. 39) of Ni/Yb_2O_3, Ni(111) and Yb_2O_3(222) planes are detected as the main crystal faces. This is consistent with the XRD patterns of Ni and Yb_2O_3, where Ni(111) and Yb_2O_3(222) planes show the strongest diffraction peaks (Supplementary Fig. 7a), respectively. The Ni(111) and Yb_2O_3(222) planes are connected in different angles, where the clear phase boundaries are found (Supplementary Fig. 39). In the magnified HRTEM image of Ni/Yb_2O_3, the lattice fringes of Ni(111) and Yb_2O_3(222) planes are arranged in parallel, between which an interface is observed (Fig. 3e). Line-scanning intensity profile obtained from the blue dashed boxes in Supplementary Fig. 39i enables us to distinguish the Ni and Yb atoms clearly based on their obviously different intensities, that is, the contrast intensity of Ni is much smaller than that of Yb caused by the smaller atomic number of Ni. The distance from a Ni atom to a nearby Yb atom is 0.300 nm (Supplementary Fig. 39i), which is very close to that between two adjacent Yb atoms (0.301 nm). This reveals that there are O atoms between the Ni atom and Yb atom, and thus the existence of Ni–O bonds in the interface between Ni and Yb_2O_3.

In addition, the fast Fourier transformation (FFT) pattern (Fig. 3f) also exhibits clear lattice signal of both Ni(111) and Yb_2O_3(222) planes, as well as their equivalent planes of Ni($\bar{1}11$) and Yb_2O_3($\bar{2}22$). The inversed FFT (IFFT) patterns (Fig. 3g) taken from the selected red and yellow dashed boxes in Fig. 3e reveal a near-parallel relationship of the Ni(111) and Yb_2O_3(222) planes, which also illustrates that the Yb_2O_3($\bar{2}22$) crystal faces grow along the Ni($\bar{1}11$) faces parallelly. The corresponding schematic structural diagram (Fig. 3h) shows the phase interface of Ni and Yb_2O_3 in detail, providing a deep insight into the heterostructure. Moreover, the lattice distance between Yb_2O_3($\bar{2}22$) planes (0.301 nm) is nearly one and a half times longer than that between Ni($\bar{1}11$) planes (0.204 nm). This reveals that Yb_2O_3($\bar{2}22$) planes can be regularly connected to Ni($\bar{1}11$) planes as highlighted by the red solid lines in Fig. 3h. Beyond the visual TEM images, line-scan electron energy loss spectroscopy (EELS) was taken to clarify the interface structure (Supplementary Fig. 40a), which was recorded along the red arrow in Supplementary Fig. 40b. The obtained spectrum clearly presents the distribution of Ni and its interface with Yb_2O_3. The intensity profiles extracted from the EELS spectrum illustrate both Ni L-edge and Yb M-edge signals on interface (II), which demonstrates a tight link between Ni and Yb_2O_3 (Supplementary Fig. 40c). In comparison with the bulk-phase Ni (III), a slight positive shift of Ni–O band with a higher peak intensity for the interfacial Ni L-edge peak is observed (Supplementary Fig. 40d), which further confirms the chemical links (i.e. Ni–O bonds) in the interface of Ni/Yb_2O_3
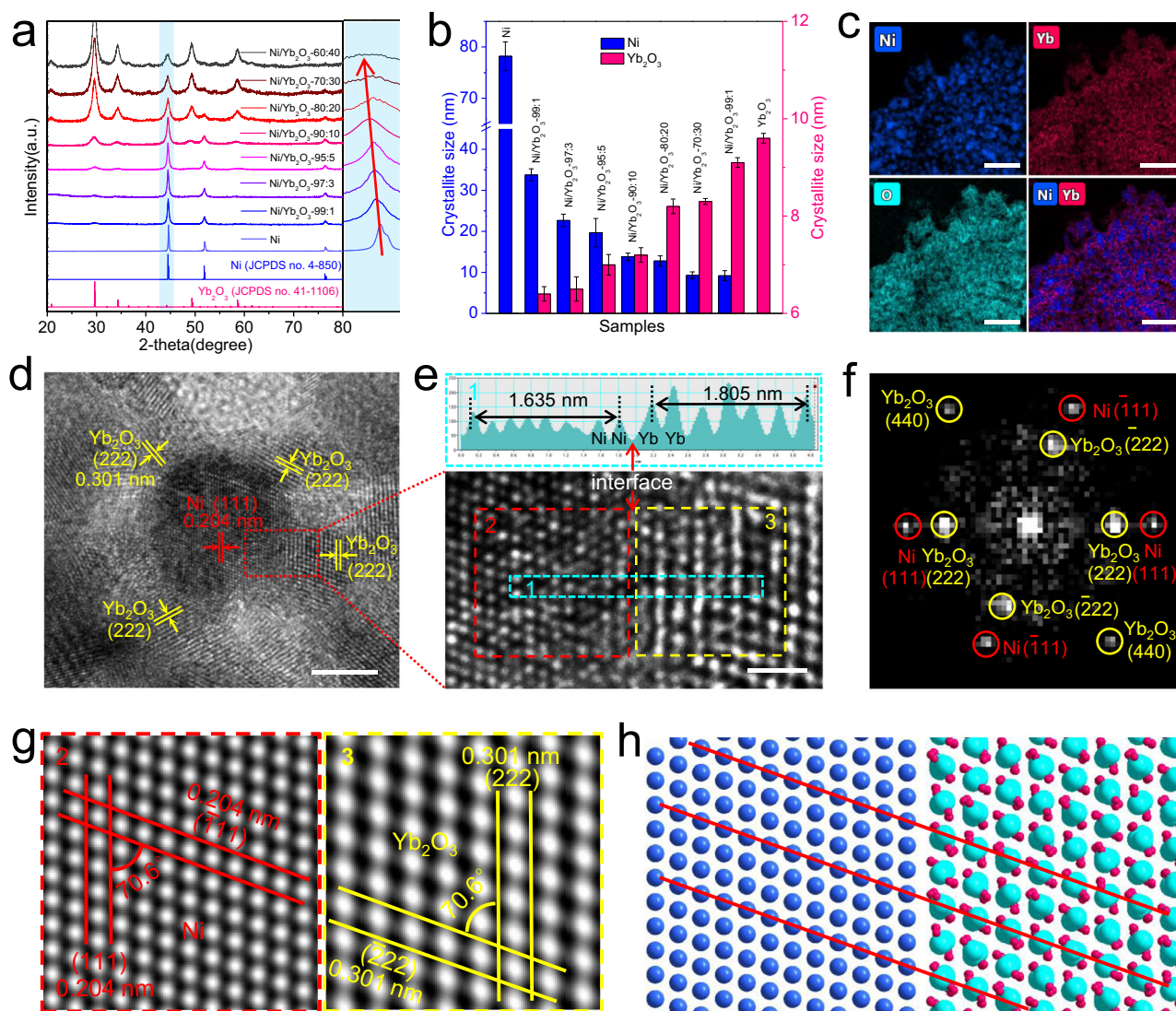
Fig. 3 Structural characterizations of Ni/Yb₂O₃. **a** XRD patterns of Ni and Ni/Yb₂O₃ hybrids with various Ni:Yb molar ratios. **b** Crystallite sizes derived from XRD patterns with the Debye–Scherrer equation. The error bars show the standard derivation based on triplicate measurements. **c** Elemental mapping of Ni/Yb₂O₃ (scale bar: 100 nm). **d**, **e** HRTEM images of Ni/Yb₂O₃ (scale bar: 5 nm for **d** and 1 nm for **e**), and line scan of HRETM image. **f** Fast Fourier transform (FFT) pattern from (**e**). **g** Inverse FFT patterns corresponding to the regions of 2 and 3 in (**e**). **h** Schematic diagram of the structures corresponding to the regions of 2 and 3 in (**e**). The blue, magenta, and cyan spheres represent the Ni, O, and Yb atoms, respectively.

hybrid. For comparison, the Ni/CeO₂ nanoparticle on graphitic plate was also synthesized by the same method (Supplementary Fig. 41).

X-ray absorption spectroscopy (XAS) and XPS were used to explore the impact of coupling Yb₂O₃ on the chemical environments and electronic structures of Ni. Figure 4a presents the X-ray absorption near-edge structure (XANES) spectra of Ni/Yb₂O₃ at Ni K-edge, which is consistent with that of the pristine Ni and Ni foil reference, revealing the retentive metallic Ni in Ni/Yb₂O₃. The near-edge adsorption energy of Ni in Ni/Yb₂O₃ shifts to a higher binding energy compared with that of the pristine Ni (Fig. 4a inset), which indicates that the Ni nanoparticles in Ni/Yb₂O₃ are partly positively charged and the electrons are transferred from Ni to Yb₂O₃. This significant electron transfer also reveals the strong coupling between Ni and Yb₂O₃, which agrees with the strong interfacial contacts between Ni and Yb₂O₃ (Fig. 3e). To further trace the radial structure function around Ni, the extended X-ray absorption fine-structure (EXAFS) spectra of Ni/Yb₂O₃ and Ni were in-depth analyzed. A prominent Fourier

transforms peak of Ni/Yb₂O₃ at 2.41 Å in R space plot is clearly observed for the Ni–Ni path, which is similar to the pristine Ni (Fig. 4b). The results from EXAFS wavelet transform show only one intensity maximum at ca. 8.2 Å⁻¹ in k space, corresponding to the Ni–Ni bond in Ni, which further confirms the metallic state of Ni in Ni/Yb₂O₃ (Fig. 4c). The decrease of Ni–Ni peak intensity in Ni/Yb₂O₃ compared with that in pristine Ni manifests the damped coordination structure of Ni (Fig. 4b)[49]. The Ni K-edge EXAFS fitting (Supplementary Table 4) indicates that the first-shell Ni–Ni coordination numbers (CNs) reduce from Ni to Ni/Yb₂O₃. The lower CN can be ascribed to the smaller crystal sizes and rich surface steps of Ni nanoparticles in the hybrid[50], which can increase the catalytic active sites and adjust the adsorption ability of Ni/Yb₂O₃. The normalized Yb L-edge XANES spectrum for Ni/Yb₂O₃ is consistent with that for the as-synthesized Yb₂O₃ (Fig. 4d). Also, the results from FT-EXAFS and EXAFS wavelet transform suggest that the Yb component in Ni/Yb₂O₃ possesses a similar coordination environment to that in pristine Yb₂O₃ (Fig. 4e, f).
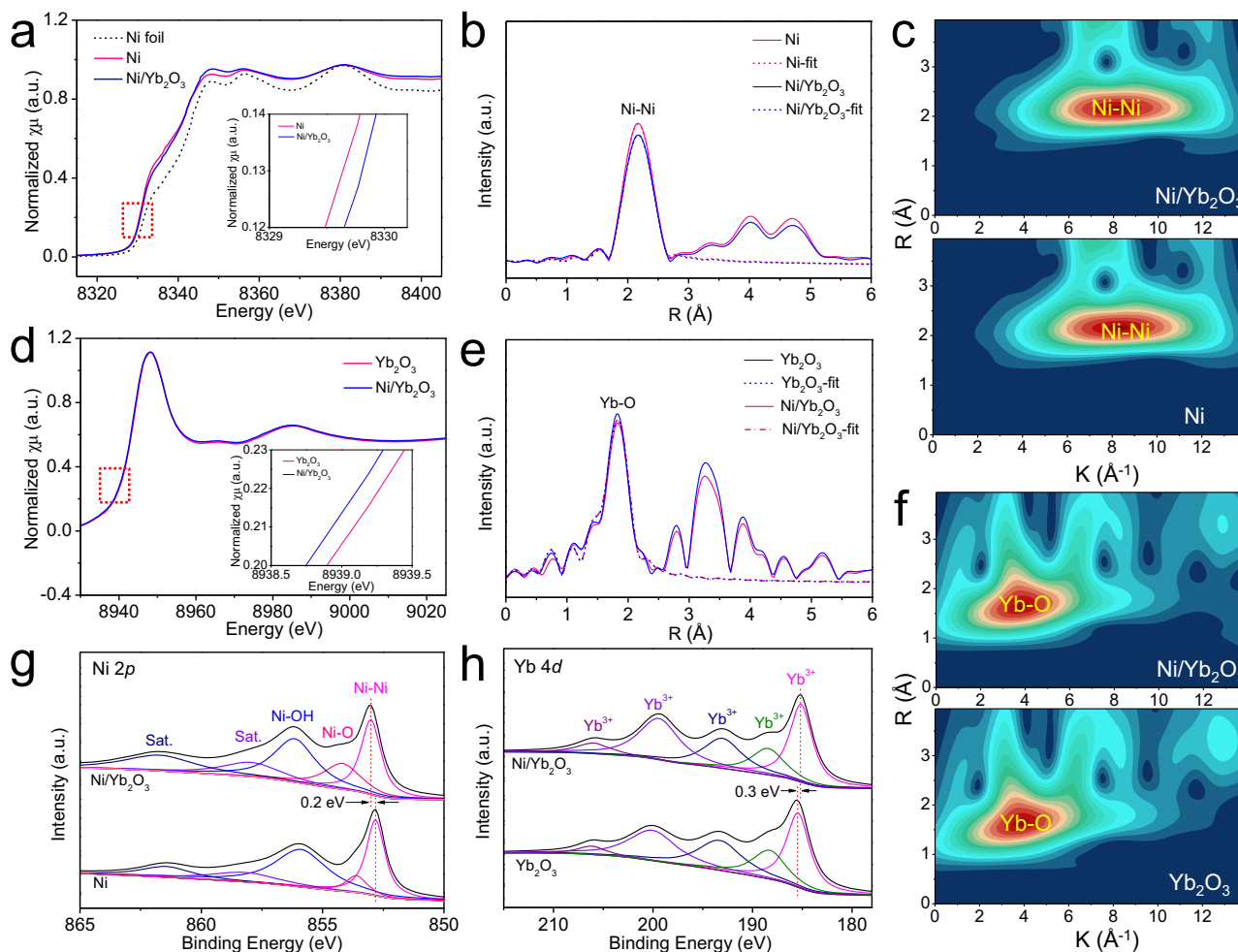
Fig. 4 Spectroscopic characterizations of Ni/Yb$_2$O$_3$ hybrid. a Ni K-edge XANES spectra of Ni/Yb$_2$O$_3$, pristine Ni, and Ni foil reference. **b, c** Fourier transforms and wavelet transforms of EXAFS spectra for Ni/Yb$_2$O$_3$ and pristine Ni. **d** Yb L-edge XANES spectra of Ni/Yb$_2$O$_3$ and pristine Yb$_2$O$_3$. **e, f** Fourier transforms and wavelet transforms of EXAFS spectra for Ni/Yb$_2$O$_3$ and pristine Yb$_2$O$_3$. **g** Ni 2*p* XPS spectra of Ni/Yb$_2$O$_3$ and pristine Ni. **h** Yb 4*d* XPS spectra of Ni/Yb$_2$O$_3$ and pristine Yb$_2$O$_3$.

As observed in Ni 2*p* XPS spectra (Fig. 4g), in addition to the Ni–Ni bands, there are Ni–O bonds in Ni/Yb$_2$O$_3$ and pristine Ni, which is different from that no distinct first-shell of Ni–O is observed in the Ni K-edge FT-EXAFS and EXAFS wavelet transform. This is primarily because that XPS is a surface sensitive analytical technique whereas XAS in the configuration used in these experiments is a bulk technique[7]. The peak intensity of Ni–O bond (Fig. 4g) in Ni/Yb$_2$O$_3$ is obviously higher than that in metallic Ni, which illustrates the presence of Ni–O interactions between Ni and Yb$_2$O$_3$[51,52]. The positively shifted Ni 2*p* peaks of Ni (Fig. 4g) and the negatively shifted Yb 4*d* peaks (Fig. 4h) in Ni/Yb$_2$O$_3$ further illustrate the strong electronic interactions between Ni and Yb$_2$O$_3$ in interface. All these results indicate that the introduction of Yb$_2$O$_3$ can modulate the geometric and electronic structures of Ni in Ni/Yb$_2$O$_3$ hybrid, which plays a significant role on its enhanced electrocatalytic activity of HER.

Evaluation of electrocatalytic activity and stability for Ni/Yb$_2$O$_3$. Among the Ni/Yb$_2$O$_3$ electrodes with different compositions, Ni/Yb$_2$O$_3$—90:10 shows the best performances in terms of overpotential, Tafel slope, and ECSA-based specific activity (Supplementary Figs. 42–44). It can be attributed to its large ECSA, high intrinsic electrocatalytic activity, and high conductivity. As discussed above, the high ECSA of Ni/Yb$_2$O$_3$—90:10

results from its appropriate amount of Yb$_2$O$_3$. And for the intrinsic catalytic activity, incorporating oxophilic Yb$_2$O$_3$ into metallic Ni affords efficient dual active sites for both H$_2$O dissociation and H$_2$ formation. Nevertheless, the challenge to achieve the best activity of the Ni/Yb$_2$O$_3$ hybrids is that an optimal balance of H$_2$O dissociation rate and H$_2$ formation rate is needed to accelerate the overall HER kinetics through steering the proportion of Ni and Yb$_2$O$_3$ components (Supplementary Fig. 45). As illustrated in Supplementary Fig. 45a, H$_2$O is first adsorbed on the oxophilic Yb$_2$O$_3$ in the interface, and then easily broken up into the OH and H intermediates. Then, the adsorbed H intermediate will form H$_2$ on the Ni sites through the Heyrovsky or Tafel step. As a result, the Ni/Yb$_2$O$_3$ heterosurfaces synergistically boost the Volmer step and the subsequent Heyrovsky or Tafel step of alkaline HER. However, overmuch Yb$_2$O$_3$ component will lead to insufficient Ni sites for H$_2$ formation, which also will result in excessive OH intermediate to limit the H$_2$O adsorption. On the contrary, if the Yb$_2$O$_3$ component is too less, water dissociation (i.e. Volmer step) becomes a rate-limiting step, leading to the insufficient rate of H$_{ads}$ formation. As shown in Supplementary Fig. 42b, the HER kinetics for the Ni/Yb$_2$O$_3$ hybrids is consistent with their catalytic activities, confirming that the alkaline HER activity on Ni/Yb$_2$O$_3$ is highly dependent on its proportion of Ni:Yb$_2$O$_3$. In addition, the introduction of Yb$_2$O$_3$ in metal Ni can lead to a marked reduction
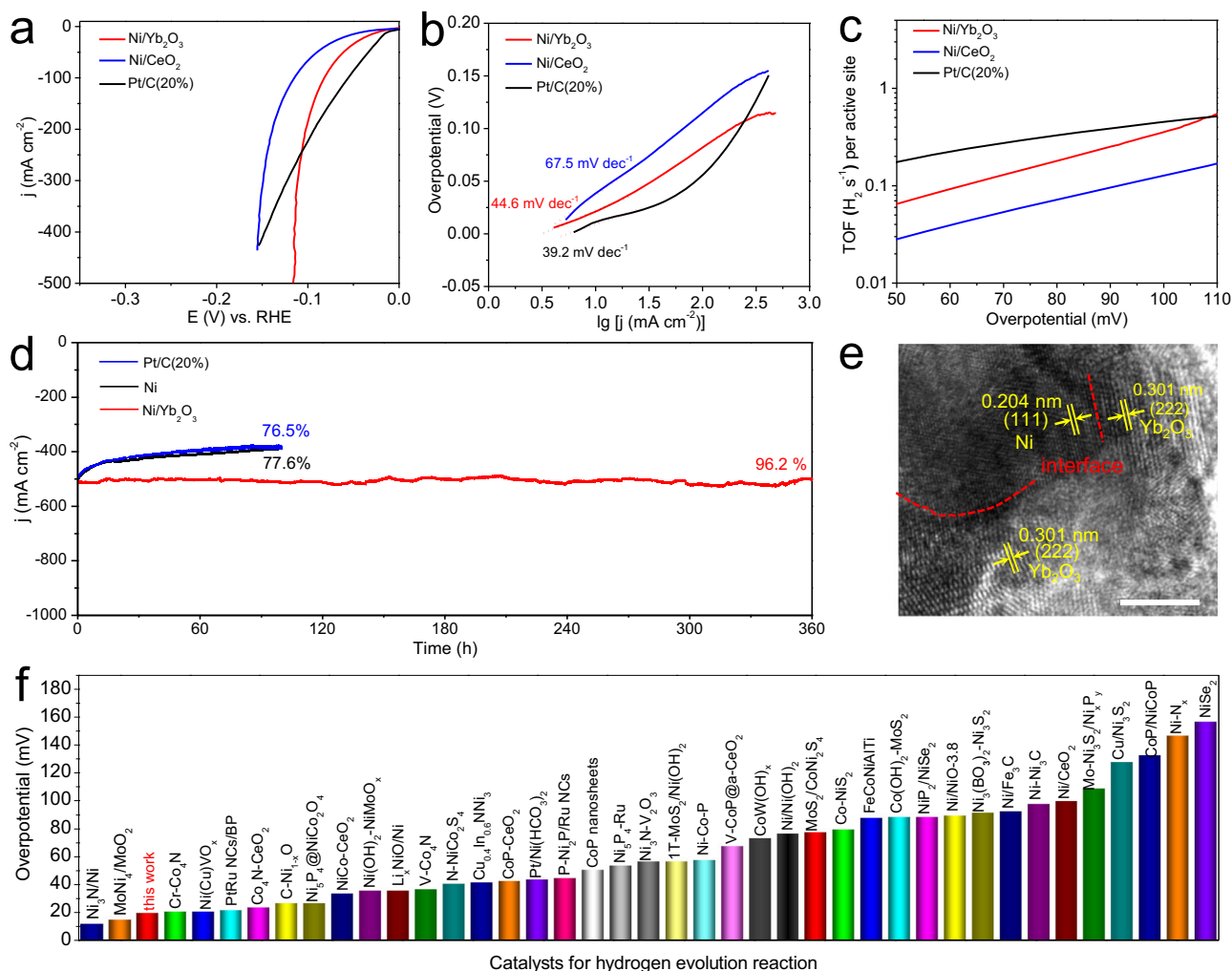
Fig. 5 Electrocatalytic HER activity and stability for Ni/Yb$_2$O$_3$ electrode in 1.0 M KOH. a Polarization curves (scan rate: 5 mV s^{-1}) of Ni/Yb$_2$O$_3$, Ni/CeO$_2$, and Pt/C(20%) electrodes with a mass loading of ca. 3.5 mg cm^{-2}. **b** Tafel plots derived from the curves in (**a**). **c** TOF values of Ni/Yb$_2$O$_3$, Ni/CeO$_2$, and Pt/C(20%) electrodes. **d** Chronopotentiometric curves of Ni/Yb$_2$O$_3$, Ni, and Pt/C(20%) electrodes at the overpotential of 116.0, 305.0, and 167.0 mV, respectively. **e** TEM image of Ni/Yb$_2$O$_3$ after the HER test. **f** Comparison of the HER activities for Ni/Yb$_2$O$_3$ and the reported electrocatalysts (Supplementary Table 6).

in conductivity of the Ni/Yb$_2$O$_3$ hybrids, caused by the very poor conductivity of Yb$_2$O$_3$ (Supplementary Fig. 46). Excessive Yb$_2$O$_3$ component will impede the electron transfer during the HER. Therefore, the 90:10 is the best molar ratio of Ni:Yb in the Ni/Yb$_2$O$_3$ hybrids.

The high alkaline HER activity of Ni/Yb$_2$O$_3$ was further evaluated by comparing with those of Ni/CeO$_2$ and Pt/C(20%). To reach the current density of 10 mA cm^{-2}, Ni/Yb$_2$O$_3$ has a small overpotential requirement of 20.0 mV (Fig. 5a and Supplementary Fig. 47). This overpotential is much lower than that of Ni/CeO$_2$ electrode (41.1 mV) and only 10.0 mV higher than that of the benchmark Pt/C(20%) electrode (Supplementary Table 5). Notably, the overpotential of Ni/Yb$_2$O$_3$ at large current density is lower than that of Pt/C(20%), suggesting its higher HER activity. This is mainly because Ni/Yb$_2$O$_3$ electrode not only has high intrinsic activity but also possesses hydrophilic self-supported electrode structure, which could ensure fast electron and mass transport at large current density[53]. As shown in Fig. 5b, the Tafel slope of Ni/Yb$_2$O$_3$ (44.6 mV dec^{-1}) is lower than that of Ni/CeO$_2$ (67.5 mV dec^{-1}) and is close to that of Pt/C(20%) (39.2 mV dec^{-1}). For Pt/C(20%) electrode, the poor contact between the physically coated Pt/C(20%) catalyst and

substrate (Supplementary Fig. 48) results in mass transfer limit at large current density, which is certified by the upward deviation at high overpotential in its Tafel plot[54]. With high catalytic activity, Ni/Yb$_2$O$_3$ only needs 116.0 mV to attain a high current density of 500 mA cm^{-2}. Moreover, the TOFs of Ni/Yb$_2$O$_3$ measured from 50 to 110 mV overpotentials are higher than those of Ni/CeO$_2$ (Fig. 5c). Notably, the TOF value of Ni/Yb$_2$O$_3$ (0.362 H$_2$ s^{-1}) is over 3 times higher than that of Ni/CeO$_2$ (0.120 H$_2$ s^{-1}) at 100 mV, which confirms that Yb$_2$O$_3$ is a better promoter of Ni catalyst for alkaline HER relative to CeO$_2$. In addition, the Faradaic efficiency of HER for Ni/Yb$_2$O$_3$ catalyst is nearly 98% (Supplementary Fig. 49).

Besides activity, stability of electrocatalysts at high current density is a critical criterion for the practical application. To evaluate the HER durability of Ni/Yb$_2$O$_3$, the continuous CV sweep was measured from 0 to −0.35 V, with Ni as a contrast. After 5000 cycles, the polarization curve of Ni shows a significant change, while Ni/Yb$_2$O$_3$ keeps the initial activity (Supplementary Fig. 50). The long-term chronoamperometry curves were also taken at an overpotential of 116.0 mV for Ni/Yb$_2$O$_3$, 305.0 mV for Ni, and 167.0 mV for Pt/C(20%). The Ni/Yb$_2$O$_3$ electrode shows excellent stability at high current density of ~500 mA cm^{-2} for

360 h, while Ni and Pt/C(20%) exhibit a rapid current decay after 100 h water electrolysis (Fig. 5d). In addition, the HER performance of Ni/Yb$_2$O$_3$ was also tested by using Hg/HgO as the reference electrode (Supplementary Fig. 51), which further confirms its high catalytic activity and stability for HER. To verify whether oxygen vacancies in Yb$_2$O$_3$ affect the electrocatalytic activity and stability, the Ni/Yb$_2$O$_3$ hybrids (Ni/Yb$_2$O$_3$—1.0 h, Ni/Yb$_2$O$_3$—2.0 h, and Ni/Yb$_2$O$_3$—4.0 h) with different oxygen vacancy concentrations were tested (Supplementary Fig. 52). The results illustrate that the three hybrids show almost identical catalytic activity and stability for alkaline HER, revealing that the performance of Ni/Yb$_2$O$_3$ hybrid are independent to the oxygen vacancies in Yb$_2$O$_3$. In terms of the overpotential at 10 mA cm^{-2} and Tafel slope, the Ni/Yb$_2$O$_3$ hybrid not only outperforms most of the Ni-based HER electrocatalysts, but also precedes most of reported alkaline HER electrocatalysts (Fig. 5f and Supplementary Table 6), manifesting its respectable catalytic activity.

The high durability of Ni/Yb$_2$O$_3$ was also confirmed by post-electrolysis characterization (Supplementary Fig. 53). The XRD pattern for Ni/Yb$_2$O$_3$ after a long-term stability test matches with the initial status before test (Supplementary Fig. 53a). The Ni/Yb$_2$O$_3$ nanoparticles are still attached onto the base tightly without morphology change (Supplementary Fig. 53b). The TEM image reveals that Ni/Yb$_2$O$_3$ remains the heterojunction structure with Yb$_2$O$_3$ decorating on the surface of Ni nanoparticles (Fig. 5e). Its corresponding element mapping illustrates the uniform distribution of Ni, Yb, and O after 360 h test (Supplementary Fig. 53c, 53d). While for Ni, an obvious oxide layer is generated on the surface of Ni nanoparticles, resulting in a Ni/NiO$_x$ core–shell structure as indicated by the TEM image, in spite of the unchanged morphology and bulk phase structure of the Ni particles (Supplementary Figs. 54a–c). The almost invisible metallic Ni content and the dominant NiO$_x$ in the XPS spectrum of Ni element also illustrate the severe oxidation of Ni (Supplementary Fig. 54d), resulting in the loss of active sites for HER, thereby the degradation of catalytic activity. As reported in previous literatures, this is an inevitable and ubiquitous problem for metallic Ni HER electrocatalysts under alkaline conditions[5,7,9]. Notably, Ni/Yb$_2$O$_3$ shows the less oxidation of Ni nanoparticles after the 360 h electrolysis operation, as illustrated by the Ni 2p XPS spectrum (Supplementary Fig. 53e). Moreover, the unaltered ECSA after HER test also indicates the high stability of Ni/Yb$_2$O$_3$ electrode (Supplementary Fig. 55). It is widely accepted that water and dissolved oxygen in the electrolyte play a major role on the corrosion of metallic Ni. Since Yb$_2$O$_3$ is highly stable under the pH and potential ranges of the HER tests, the surface anchored Yb$_2$O$_3$ can serve as the protection shell for Ni phase, preventing the oxidation of Ni phase[10,55]. Moreover, electronic interaction between Ni and Yb$_2$O$_3$ can also decrease the adsorption energy of O$_2$ on the Ni sites, thereby further relieving the oxygen corrosion. These facts are beneficial to the electrochemical stability of the Ni/Yb$_2$O$_3$ hybrid for HER at high current density. As a result, the synchronous enhancement of HER activity and stability of Ni-based materials can be achieved by coupling the Yb$_2$O$_3$ promoter. To further illustrate the interfacial effect between Ni and Yb$_2$O$_3$, a Ni + Yb$_2$O$_3$ sample was prepared by mechanically mixing Ni and Yb$_2$O$_3$ powder using Nafion as the binder. Obviously, the Ni + Yb$_2$O$_3$ catalyst shows quite inferior activity and stability compared with that of Ni/Yb$_2$O$_3$ (Supplementary Fig. 56), which reveals that the strong coupling interface between Ni and Yb$_2$O$_3$ plays a key role in the enhanced catalytic activity and stability of Ni/Yb$_2$O$_3$[56].

Theoretical simulations. The first principle calculations were used to elucidate the theoretical enhancement of intrinsic HER

activity and stability for the heterogeneous interface in Ni/Yb$_2$O$_3$ as compared with pristine Ni. First, the structural models of Ni/Yb$_2$O$_3$, pristine Ni, Yb$_2$O$_3$, and Ni/CeO$_2$ were established based on the determined structures of these materials (Supplementary Fig. 57). The energy barrier of water dissociation is a critical factor to characterize the intrinsic catalytic activity for HER in alkaline media[3,57]. As proved by the CV curves for OH adsorption and desorption experiments (Supplementary Fig. 25), the incorporation of oxophilic lanthanide oxides in metallic Ni strengthens the adsorption energy of OH. This is also verified by the first principle calculation result, that is, the adsorption energy of OH on Ni(111)/Yb$_2$O$_3$(222) is more negative than that on pure Ni (Supplementary Fig. 58). The strong adsorption of OH on Ni(111)/Yb$_2$O$_3$(222) indicates the favorable adsorption of water molecules and cleaving of HO–H bond. To validate this prediction, the energy barriers for water dissociation on catalysts were taken by density functional theory (DFT) calculation. As shown in Supplementary Fig. 59, the stronger H$_2$O adsorption on Ni/Yb$_2$O$_3$ and Ni/CeO$_2$ hybrids relative to pristine Ni further certifies that the coupling of oxophilic Yb$_2$O$_3$ and CeO$_2$ on Ni significantly promotes the adsorption of water molecules, which will expedite the water dissociation thereon[58]. The H$_2$O dissociation reaction on pure Ni surface, Yb$_2$O$_3$ surface, and interface of Ni/Yb$_2$O$_3$ and Ni/CeO$_2$ were also calculated (Fig. 6a–c and Supplementary Figs. 60–63). With regard to Ni(111)/Yb$_2$O$_3$(222) interface (Fig. 6b and Supplementary Fig. 62), the oxygen of water is absorbed on Yb of Yb$_2$O$_3$ and then the water molecule is broken up to the hydroxyl and hydrogen intermediates, which are adsorbed by Yb and nearby Ni atoms, respectively. As expected, the energy barrier for water dissociation on the interface of Ni(111)/Yb$_2$O$_3$(222) is 0.47 eV (Fig. 6c), which is dramatically lower than those on Ni(111) surface (0.62 eV) and Yb$_2$O$_3$(222) surface (1.12 eV). This result demonstrates that the sluggish water dissociation step on Ni can be greatly facilitated by coupling with Yb$_2$O$_3$, which is consistent with the Tafel slope and EIS analysis. More importantly, this energy barrier is even lower than that of Pt surface (0.56 eV)[59], and is also close to that (0.41 eV) of Ni(111)/CeO$_2$(111) interface. Thus, in addition to the well-known water dissociation promoter CeO$_2$, the bixbyite-type Yb$_2$O$_3$ with suitable oxophilicity is also a promising promoter for water dissociation. The accelerated water dissociation step of Volmer process on Ni(111)/Yb$_2$O$_3$(222) provides enough hydrogen intermediate to the active Ni sites for subsequent Heyrovsky step or Tafel step.

Except for the energy barrier of water dissociation, the free adsorption energy of H* (ΔG_{H*}) is another important descriptor to characterize the alkaline HER activities of electrocatalysts. High-efficiency HER electrocatalysts should possess moderate H* adsorption energy[60]. As for the charge density difference (Fig. 6d), the increased charge densities are clearly represented at the Ni/Yb$_2$O$_3$ interface. This implies strong synergistic interactions between Ni and Yb$_2$O$_3$ in hybrid, which play a vital role in promoting the electron transfer. The differential charge density analysis also reveals that the electron transfer occurs from Ni to O in the Ni/Yb$_2$O$_3$ interface, which thus renders the lowered d-band center of the interfacial Ni atom in Ni/Yb$_2$O$_3$ (Fig. 6e) and reduces the strong adsorption energy of H on metallic Ni[61]. Figure 6f shows the calculated ΔG_{H*} on bare Ni(111), bare Yb$_2$O$_3$(222), Ni(111)/Yb$_2$O$_3$(222) and Ni(111)/CeO$_2$(111) with most energetically stable configurations (Supplementary Fig. 64). With regard to pristine Ni and Yb$_2$O$_3$, the ΔG_{H*} are calculated to be −0.38 and −2.43 eV, respectively, which indicate the strong adsorption of H on these sites. This will prevent the H* desorption and H$_2$ generation, resulting in the poor HER reaction kinetics[61]. As anticipated, coupling Ni with Yb$_2$O$_3$ significantly optimizes the ΔG_{H*} of Ni (−0.26 eV). The reduced but
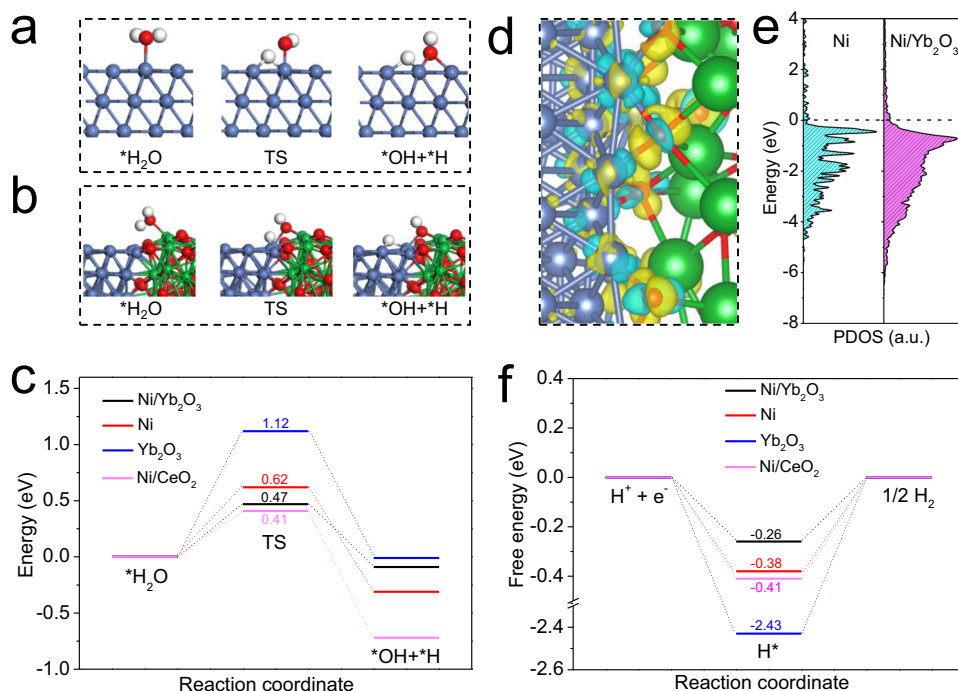
Fig. 6 Theoretical simulations. a Atomic configurations of simulated H_2O dissociation process on the optimized sites of pristine Ni(111) surface. **b** Atomic configurations of simulated water dissociation process on the optimized sites of Ni(111)/Yb_2O_3(222) interface. **c** Kinetic barrier of water dissociation on Ni(111)/Yb_2O_3(222), Ni(111), Yb_2O_3(222) and Ni(111)/CeO_2(111). **d** Difference of charge density for Ni(111)/Yb_2O_3(222) with the isosurface = 0.004 e bohr^{-3} (yellow and cyan shadows show electron accumulation and electron depletion, respectively). **e** Partial density of states (PDOS) of Ni in pristine Ni and Ni/Yb_2O_3. **f** Calculated ΔG_{H*} for Ni(111)/Yb_2O_3(222), Ni(111), Yb_2O_3(222), and Ni(111)/CeO_2(111) systems. The blue, red, white, and green spheres represent the Ni, O, H, and Yb atoms, respectively.

optimized H binding energy of Ni/Yb_2O_3 would favor the transformation of H* to H_2, and also expedite the H_2 desorption to refresh the catalytic active sites. It is worth noting that the doped CeO_2 is inferior in optimizing the H binding energy of Ni and the Ni/CeO_2 hybrid still shows the strong H binding energy that is similar to the pristine Ni. This impedes the subsequent Heyrovsky or Tafel step, although the lowered energy barrier of water dissociation (Volmer step) is obtained on the Ni(111)/CeO_2(111) hybrid. Remarkably, coupling Yb_2O_3 with Ni can concurrently lower the H_2O-dissociation energy barrier and optimize the $\triangle G_{H*}$, thereby promoting the kinetics of HER in alkaline medium as experimentally observed.

In fact, there are two kinds of Ni sites in the Ni/Yb_2O_3 hybrids, including the interfacial Ni sites coupling with Yb_2O_3 and the other Ni sites far from interfaces (Supplementary Fig. 45a). Due to the lack of effective sites for water dissociation, the energy barriers of water dissociation on the Ni sites far from Ni/Yb_2O_3 interface (0.61 eV) is almost identical to that of pure Ni (0.62 eV), which is clearly higher than that (0.47 eV) of the Ni/Yb_2O_3 interface (Supplementary Figs. 65 and 66a). The $\triangle G_{H*}$ on the Ni sites far from Ni/Yb_2O_3 interface (−0.39 eV) is also similar to that (−0.38 eV) on pure Ni (Supplementary Figs. 66b and 67), since the far distance limits the electronic interactions between these non-interface Ni sites and Yb_2O_3[62]. This result indicates that the Ni site far from Ni/Yb_2O_3 interface has low catalytic activity and the heterogeneous interface is the catalytic active center of Ni/Yb_2O_3, on which the alkaline HER occurs preferentially and rapidly. Additionally, the Ni sites far from Ni/CeO_2 interface also display the analogous energy barriers of water dissociation and $\triangle G_{H*}$ with pure Ni (Supplementary Figs. 66–68), further confirming their low activity.

Generally, metallic Ni is easily subject to oxidation by oxygen dissolved in the electrolyte or oxygen migrated from the counter

electrodes, resulting in the loss of active sites. The stability experiments and the post-electrolysis characterizations verify that Yb_2O_3 coupling could relieve the oxidation corrosion of Ni, thereby improving the stability of Ni/Yb_2O_3 for catalyzing HER. Furthermore, the DFT calculations illustrate that the adsorption energies of O_2 on different Ni adsorption sites of Ni/Yb_2O_3 are much weaker than that on bare Ni surface (Supplementary Fig. 69). This suggests that the Ni phase in Ni/Yb_2O_3 is more resistant to O_2 interaction and oxidation erosion than pure Ni[63], which ensures the highly active heterojunction of Ni and Yb_2O_3 during the HER process. Moreover, the lowered H binding energy on Ni of Ni/Yb_2O_3 can decrease the hydrogen-adsorption poison of Ni active sites, thus improving its long-term stability for HER[64].

Discussion

In summary, the enhancement effect of bixbyite-type lanthanide sesquioxides for alkaline HER performances has been proposed and validated based on the designed Ni/Ln_2O_3 model catalysts. The screened Ni/Yb_2O_3 not only exhibits the best HER catalytic performances in the diverse Ni/Ln_2O_3 hybrids, but also outperforms the well-known Ni/CeO_2 electrocatalyst, revealing that Yb_2O_3 is a better performance enhancer of Ni for alkaline HER relative to the traditional CeO_2. Incorporating oxophilic Yb_2O_3 into metallic Ni affords the dual active sites, greatly accelerating the dissociation of water, and the localized electronic polarization between Ni and Yb_2O_3 optimizes the hydrogen adsorption energy, thus boosting the overall HER kinetics. In addition, the tightly coupled Yb_2O_3 with high chemical stability significantly lowers the grain sizes and inhibits the chemical oxidation corrosion of Ni, resulting in enlarged ECSA and robust stability. Remarkably, the Ni/Yb_2O_3 electrode exhibits an ultralow overpotential of 20.0 mV at 10 mA cm^{-2} and retains the high stability

over 360 h at a large current density of 500 mA cm^{-2}, preceding most of the reported alkaline HER catalysts. The high activity and durability endow the Ni/Yb$_2$O$_3$ electrode with great potentials in large-scale application for industrial electrolyzer. More significantly, the ability of Ln$_2$O$_3$ to promote the water dissociation should not be limited to alkaline HER system, which will be also available to other catalytic reactions involving water dissociation. The applications of these promising Ln$_2$O$_3$ promoters toward those electrocatalytic processes, such as CO$_2$RR, NRR, ORR, and water–gas shift (WGS), are underway.

Methods

Preparation of materials. For the preparation of a Ni/Ln$_2$O$_3$ electrode, the graphite plate (1 × 2 cm^2) was cleaned in ethanol, dilute HCl and ultrapure water, respectively, then dried at room temperature. The precursor was prepared by the electrodeposition method in an electrolytic cell with graphite plate as working electrode. The deposited electrolyte is a water solution of 0.09 M Ni(NO$_3$)$_2$ and 0.01 M Ln(NO$_3$)$_3$. During the electrodeposition process of Ni(OH)$_2$/Ln(OH)$_3$, the GP was treated at 20 mA cm^{-2} for 600 s and then −40 mA cm^{-2} for 600 s. Subsequently, the deposited Ni(OH)$_2$/Ln(OH)$_3$ was converted to Ni/Ln$_2$O$_3$ in a tube furnace at 500 °C under 10% H$_2$/Ar mixture for 4 h with a heating rate of 5 °C min^{-1}. For comparison, Ni/Yb$_2$O$_3$ with different Ni:Yb molar ratios (i.e. 99:1, 97:3, 95:5, 90:10, 80:20, 70: 30, and 60:40) were synthesized by adjusting the amount of Ni(NO$_3$)$_2$ and Yb(NO$_3$)$_3$. In addition, the Ni and Ln$_2$O$_3$ electrodes were prepared by a similar method, using only 0.1 M Ni(NO$_3$)$_2$ or 0.1 M Ln(NO$_3$)$_3$, respectively. The Ni/CeO$_2$ electrode was also prepared by this method for a comparison. The catalyst loading for each electrode is ca. 3.5 mg cm^{-2}.

Characterizations of materials. Powder XRD measurements were taken on a Rigaku model Ultima IV diffractometer with Cu-Kα X-ray source. SEM images were collected on a FEI Nova Nano 230 scanning electron microscope. TEM equipped with EDS and SAED was conducted on a Tecnai G^2 F20 electron microscope. XPS was measured by a Kratos Axis Ultra DLD spectrometer. Inductively coupled plasma atomic emission spectrometer (ICP-AES) was performed on PerkinElmer Optima 83000. X-ray absorption fine structure spectra (Ni K-edge/Yb L-edge) were collected at BL14W beamline in Shanghai Synchrotron Radiation Facility (SSRF). The storage rings of SSRF were operated with a stable current of 200 mA at 3.5 GeV. With Si(111) double-crystal monochromator, the data collection was taken in Transmission mode using Lytle detector under ambient conditions.

Electrochemical measurements. Electrochemical measurements were performed in a three-electrode cell with a volume of 150 mL using the Bipotentiostat workstation (Pine Research Instrumentation, Basic Wave Driver 20 Bundle, USA) and Solartron ModuLab XM. The as-prepared self-supported electrode was used as the working electrode. The area of as-prepared electrode is 2.0 cm^2, of which the part loading catalyst immersed into the electrolyte is 1.0 cm^2 (Supplementary Fig. 2). The Pt/C(20%)@GP electrode was prepared by drop casting Pt/C(20%) catalyst ink on GP (3.5 mg cm^{-2}). The ink was achieved by ultrasonically dispersing 10 mg Pt/C(20%) in a mixed solution containing 950 μL ethanol and 50 μL Nafion solution. A 1.0 M KOH solution purged with Ar gas was applied as the electrolyte. The LSV from 0.1 to −0.5 V were recorded at a rate of 5 mV s^{-1}. EIS measurements were taken in the frequency region from 100 kHz to 0.01 Hz. The amounts of produced H$_2$ were collected using the drainage route. The Faradic efficiency was defined as the ratio of experimental H$_2$ production amount to theoretical H$_2$ production amount. The RHE calibration of reference electrode was taken in H$_2$-saturated 1 M KOH using a platinum plate as the working electrode (Supplementary Figs. 51a, 70). All potentials were reported relative to the RHE scale unless noted. All polarization curves were iR-corrected using: $E_{iR} = E_{tested} - i \times 0.8R_s$ (R_s is resistance of system).

Computational methods. The DFT calculations were performed by Vienna Ab-initio Simulation Package (VASP)[65]. The ion–electron interaction was described by using the projector-augmented wave (PAW) method[66]. The electron exchange-correlation was revealed by the functions of Perdew, Burke, and Ernzerhof (PBE) of generalized gradient approximation (GGA)[67]. The DFT-D3 method was taken to describe the van der Waals correction. For all calculations, the cutoff energy was set to be 520 eV. Furthermore, the periodic boundary conditions with the vacuum slab of 15 Å were used to avoid the interactions between neighboring periodic structures. A 3 × 3 × 1 Monkhorst–Pack grid was used for all calculations[68]. The convergence threshold for the geometry optimization was set to 10^{-5} eV in energy and 0.01 eV Å^{-1} in force, respectively. The convergence threshold in force for transition state searching calculations was set to 0.05 eV Å^{-1}. The climbing image nudged elastic band (CI-NEB) method was taken to search the minimum energy pathway (MEP) for water dissociating into OH and H radical[69]. The H$_2$O

absorption energy was calculated by Eq. (3):

$$\Delta E_{H_2O} = E_{(surf+H_2O)} - E_{(surf)} - E_{H_2O} \qquad (3)$$

where $E_{(surf+H_2O)}$ and $E_{(surf)}$ are the energies of the surfaces with and without H$_2$O adsorbate, respectively. E_{H_2O} is the energy of a H$_2$O molecule. The free energy change (ΔG) of adsorbate is calculated according to Eq. (4):

$$\Delta G = \Delta E + \Delta E_{ZPE} - T\Delta S \qquad (4)$$

in which ΔE is DFT calculated total energy change, ΔE$_{ZPE}$ is the zero-point energy change, and ΔS is the entropy difference.

Data availability

All data generated in this study are provided in the Supplementary Information/Source Data file. Source data are provided with this paper.

References

1. Lu, B. et al. Ruthenium atomically dispersed in carbon outperforms platinum toward hydrogen evolution in alkaline media. *Nat. Commun.* **10**, 631 (2019).
2. Fan, J. et al. Hydrogen stabilized RhPdH 2D bimetallene nanosheets for efficient alkaline hydrogen evolution. *J. Am. Chem. Soc.* **142**, 3645–3651 (2020).
3. Zang, Y. et al. Tuning orbital orientation endows molybdenum disulfide with exceptional alkaline hydrogen evolution capability. *Nat. Commun.* **10**, 1217 (2019).
4. Kou, T. et al. Carbon doping switching on the hydrogen adsorption activity of NiO for hydrogen evolution reaction. *Nat. Commun.* **11**, 590 (2020).
5. Gong, M., Wang, D. Y., Chen, C. C., Hwang, B. J. & Dai, H. A mini review on nickel-based electrocatalysts for alkaline hydrogen evolution reaction. *Nano Res.* **9**, 28–46 (2015).
6. Zhao, L. et al. Steering elementary steps towards efficient alkaline hydrogen evolution via size-dependent Ni/NiO nanoscale heterosurfaces. *Natl Sci. Rev.* **7**, 27–36 (2020).
7. Li, Y. et al. Implanting Ni–O–VO$_x$ sites into Cu-doped Ni for low-overpotential alkaline hydrogen evolution. *Nat. Commun.* **11**, 2720 (2020).
8. Hall, D. S., Bock, C. & MacDougall, R. R. The electrochemistry of metallic nickel: oxides, hydroxides, hydrides and alkaline hydrogen evolution. *J. Electrochem. Soc.* **160**, 235 (2013).
9. Gong, M. et al. Nanoscale nickel oxide/nickel heterostructures for active hydrogen evolution electrocatalysis. *Nat. Commun.* **5**, 4695 (2014).
10. Gong, M. et al. Blending Cr$_2$O$_3$ into a NiO–Ni electrocatalyst for sustained water splitting. *Angew. Chem. Int. Ed.* **54**, 11989–11993 (2015).
11. Subbaraman, R. et al. Enhancing hydrogen evolution activity in water splitting by tailoring Li$^+$–Ni(OH)$_2$-Pt interfaces. *Science* **334**, 1256–1260 (2011).
12. Lao, M. et al. Platinum/nickel bicarbonate heterostructures towards accelerated hydrogen evolution under alkaline conditions. *Angew. Chem. Int. Ed.* **58**, 5432–5437 (2019).
13. Lu, K. et al. Li$_x$NiO/Ni Heterostructure with strong basic lattice oxygen enables electrocatalytic hydrogen evolution with Pt-like activity. *J. Am. Chem. Soc.* **142**, 12613–12619 (2020).
14. Ruqia, B. & Choi, S. Catalytic surface specificity on Pt and Pt-Ni(OH)$_2$ electrodes for the hydrogen evolution reaction in alkaline electrolytes and their nano-scaled electro-catalysts. *ChemSusChem* **11**, 2643–2653 (2018).
15. Xue, S. et al. Enhancing the hydrogen evolution reaction activity of platinum electrodes in alkaline media using nickel-iron clusters. *Angew. Chem. Int. Ed.* **59**, 10934–10938 (2020).
16. Luo, Y. et al. Two-dimensional MoS$_2$ confined Co(OH)$_2$ electrocatalysts for hydrogen evolution in alkaline electrolytes. *ACS Nano* **12**, 4565–4573 (2018).
17. Xiao, X. et al. In situ growth of Ru nanoparticles on (Fe,Ni)(OH)$_2$ to boost hydrogen evolution activity at high current density in alkaline media. *Small Methods* **4**, 1900796 (2020).
18. Dai, L. et al. Ultrathin Ni(0)-embedded Ni(OH)$_2$ heterostructured nanosheets with enhanced electrochemical overall water splitting. *Adv. Mater.* **32**, 1906915 (2020).
19. Huang, J. et al. Boosting hydrogen transfer during Volmer reaction at oxides/metal nanocomposites for efficient alkaline hydrogen evolution. *ACS Energy Lett.* **4**, 3002–3010 (2019).
20. Hu, C. et al. In situ electrochemical production of ultrathin nickel nanosheets for hydrogen evolution electrocatalysis. *Chem* **3**, 122–133 (2017).

21. Wang, J. et al. The application of CeO₂-based materials in electrocatalysis. *J. Mater. Chem. A* **7**, 17675–17702 (2019).

22. Li, Q. et al. A review on CeO₂-based electrocatalyst and photocatalyst in energy conversion. *Adv. Energy Sustain. Res.* **2**, 200063 (2021).

23. Wu, K., Sun, L. D. & Yan, C. H. Recent progress in well-controlled synthesis of ceria-based nanocatalysts towards enhanced catalytic performance. *Adv. Energy Mater.* **6**, 1600501 (2016).

24. Sun, H. et al. Boosting activity on Co₄N porous nanosheet by coupling CeO₂ for efficient electrochemical overall water splitting at high current densities. *Adv. Funct. Mater.* **30**, 1910596 (2020).

25. Yang, F. et al. Boosting hydrogen oxidation activity of Ni in alkaline media through oxygen-vacancy-rich CeO₂/Ni heterostructures. *Angew. Chem. Int. Ed.* **58**, 14179–14183 (2019).

26. Xia, J. et al. Efficient optimization of electron/oxygen pathway by constructing ceria/hydroxide interface for highly active oxygen evolution reaction. *Adv. Funct. Mater.* **30**, 1908367 (2020).

27. Sivanantham, A., Ganesan, P. & Shanmugam, S. A synergistic effect of Co and CeO₂ in nitrogen-doped carbon nanostructure for the enhanced oxygen electrode activity and stability. *Appl. Catal. B-Environ.* **237**, 1148–1159 (2018).

28. Xu, H., Wang, A. L., Tong, Y. & Li, G. R. Enhanced catalytic activity and stability of Pt/CeO₂/PANI hybrid hollow nanorod arrays for methanol electro-oxidation. *ACS Catal.* **6**, 5198–5206 (2016).

29. Rezvani, A. et al. CO₂ reduction to methanol on Au/CeO₂ catalysts: mechanistic insights from activation/deactivation and SSITKA measurements. *ACS Catal.* **10**, 3580–3594 (2020).

30. Lv, C. et al. An amorphous noble-metal-free electrocatalyst that enables nitrogen fixation under ambient conditions. *Angew. Chem. Int. Ed.* **57**, 6073–6076 (2018).

31. Weng, Z. et al. Metal/oxide interface nanostructures generated by surface segregation for electrocatalysis. *Nano Lett.* **15**, 7704–7710 (2015).

32. Yang, L., Liu, R. & Jiao, L. Electronic redistribution: construction and modulation of interface engineering on CoP for enhancing overall water splitting. *Adv. Funct. Mater.* **30**, 1909618 (2020).

33. Zhang, R. et al. Selective phosphidation: an effective strategy toward CoP/CeO₂ interface engineering for superior alkaline hydrogen evolution electrocatalysis. *J. Mater. Chem. A* **6**, 1985–1990 (2018).

34. Sun, H. et al. Coupling NiCo alloy and CeO₂ to enhance electrocatalytic hydrogen evolution in alkaline solution. *Adv. Sustain. Syst.* **4**, 2000122 (2020).

35. Pavlik, A. III, Ushakov, S. V., Navrotsky, A., Benmore, C. J. & Weber, R. J. K. Structure and thermal expansion of Lu₂O₃ and Yb₂O₃ up to the melting points. *J. Nucl. Mater.* **495**, 385–391 (2017).

36. Yan, Z. et al. Anion insertion enhanced electrodeposition of robust metal hydroxide/ oxide electrodes for oxygen evolution. *Nat. Commun.* **9**, 2373 (2018).

37. Sun, H. et al. Superhydrophilic amorphous Co-B-P nanosheet electrocatalysts with Pt-like activity and durability for the hydrogen evolution reaction. *J. Mater. Chem. A* **6**, 22062–22069 (2018).

38. Wang, J. et al. Non-precious-metal catalysts for alkaline water electrolysis: operando characterizations, theoretical calculations, and recent advances. *Chem. Soc. Rev.* **49**, 9154–9196 (2020).

39. Wang, X. et al. Strategies for design of electrocatalysts for hydrogen evolution under alkaline conditions. *Mater. Today* **36**, 125–138 (2020).

40. Hu, C., Zhang, L. & Gong, J. Recent progress made in the mechanism comprehension and design of electrocatalysts for alkaline water splitting. *Energy Environ. Sci.* **12**, 2620–2645 (2019).

41. Nikolic, V. M. et al. Kinetics of hydrogen evolution reaction in alkaline electrolysis on a Ni cathode in the presence of Ni–Co–Mo based ionic activators. *Appl. Catal. B-Environ.* **179**, 88–94 (2015).

42. Xie, C. et al. In-situ phase transition of WO₃ boosting electron and hydrogen transfer for enhancing hydrogen evolution on Pt. *Nano Energy* **71**, 104653 (2020).

43. Mao, B. et al. Identifying the transfer kinetics of adsorbed hydroxyl as a descriptor. *Angew. Chem. Int. Ed.* **59**, 15232–15237 (2020).

44. Subbaraman, R. et al. Trends in activity for the water electrolyser reactions on 3d M(Ni,Co,Fe,Mn) hydr(oxy)oxide catalysts. *Nat. Mater.* **11**, 550–557 (2012).

45. Wei, C. et al. Surface composition dependent ligand effect in tuning the activity of nickel-copper bimetallic electrocatalysts toward hydrogen evolution in alkaline. *J. Am. Chem. Soc.* **142**, 7765–7775 (2020).

46. Kim, J. et al. Tailoring binding abilities by incorporating oxophilic transition metals on 3D nanostructured Ni arrays for accelerated alkaline hydrogen evolution reaction. *J. Am. Chem. Soc.* **143**, 1399–1408 (2021).

47. Carrasco, J. et al. In situ and theoretical studies for the dissociation of water on an active Ni/CeO₂ catalyst: importance of strong metal-support interactions for the cleavage of O–H bonds. *Angew. Chem. Int. Ed.* **54**, 3917–3921 (2015).

48. Liu, Z. et al. Ambient pressure XPS and IRRAS investigation of ethanol steam reforming on Ni–CeO₂(111) catalysts: an in situ study of C–C and O–H bond scission. *Phys. Chem. Chem. Phys.* **54**, 16621–16628 (2016).

49. Chen, X. et al. Boosting electrocatalytic oxygen evolution by cation defect modulation via electrochemical etching. *CCS Chem.* **3**, 675–685 (2020).

50. Duan, Y. et al. Bimetallic nickel–molybdenum–tungsten nanoalloys for high-efficiency hydrogen oxidation catalysis in alkaline electrolytes. *Nat. Commun.* **11**, 4789 (2020).

51. Guo, Y. et al. Low-temperature CO₂ methanation over CeO₂-supported Ru single atoms, nanoclusters, and nanoparticles competitively tuned by strong metal–support interactions and H-spillover effect. *ACS Catal.* **8**, 6203–6215 (2018).

52. Resasco, J. et al. Uniformity is key in defining structure–function relationships for atomically dispersed metal catalysts: the case of Pt/CeO₂. *J. Am. Chem. Soc.* **142**, 169–184 (2020).

53. Sun, H. et al. Self-supported transition-metal-based electrocatalysts for hydrogen and oxygen evolution. *Adv. Mater.* **32**, 1806326 (2020).

54. Sun, H. et al. Porous multishelled Ni₂P hollow microspheres as active electrocatalyst for hydrogen and oxygen evolution. *Chem. Mater.* **29**, 8539–8547 (2017).

55. Obata, K. & Takanabe, K. A permselective CeOₓ coating improves the stability of oxygen evolution electrocatalysts. *Angew. Chem. Int. Ed.* **57**, 1616–1620 (2018).

56. Wang, T., Gao, X. & Jiao, L. Ni₂P/NiMoP heterostructure as a bifunctional electrocatalyst for energy-saving hydrogen production. *eScience* **1**, 67–74 (2021).

57. He, Q. et al. Achieving efficient alkaline hydrogen evolution reaction over a Ni₅P₄ catalyst incorporating single-atomic Ru sites. *Adv. Mater.* **32**, 1906972 (2020).

58. Jiang, X. et al. Heterostructure of Ru₂P/WO₃/NPC synergistically promotes H₂O dissociation for improved hydrogen evolution. *Angew. Chem. Int. Ed.* **60**, 4110–4116 (2021).

59. Jiang, K. et al. Single platinum atoms embedded in nanoporous cobalt selenide as electrocatalyst for accelerating hydrogen evolution reaction. *Nat. Commun.* **10**, 1743 (2019).

60. Sun, Y. et al. Modulating electronic structure of metal-organic frameworks by introducing atomically dispersed Ru for efficient hydrogen evolution. *Nat. Commun.* **12**, 1369 (2021).

61. Sun, L. et al. Modification of the intermediate binding energies on Ni/Ni₃N heterostructure for enhanced alkaline hydrogen oxidation reaction. *Adv. Funct. Mater.* **31**, 2106156 (2021).

62. Lykhach, Y. et al. Counting electrons on supported nanoparticles. *Nat. Mater.* **15**, 284–288 (2016).

63. Huang, J. et al. The underlying molecular mechanism of fence engineering to break the activity-stability trade-off of catalysts. *Angew. Chem. Int. Ed.* **61**, e202114899 (2022).

64. Soares, D. E., Kleinke, M. U., Torriani, I. & Teschke, O. Deactivation mechanism of nickel cathodes in alkaline media. *Int. J. Hydrog. Energy* **7**, 573–578 (1994).

65. Kresse, G. & Furthmüller, J. Efficient iterative schemes for ab initio total-energy calculations using a plane-wave basis set. *Phys. Rev. B* **54**, 11169 (1996).

66. Blöchl, P. E. Projector augmented-wave method. *Phys. Rev. B* **50**, 17953–17979 (1994).

67. Hammer, B., Hansen, L. B. & Nørskov, J. K. Improved adsorption energetics within density-functional theory using revised Perdew–Burke–Ernzerhof functionals. *Phys. Rev. B* **59**, 7413–7421 (1999).

68. Monkhorst, H. J. & Pack, J. D. Special points for Brillouin-zone integrations. *Phys. Rev. B* **13**, 5188–5192 (1976).

69. Henkelman, G., Uberuaga, B. P. & Jónsson, H. A climbing image nudged elastic band method for finding saddle points and minimum energy paths. *J. Chem. Phys.* **113**, 9901–9904 (2000).

Acknowledgements

Author contributions

H.-S. and M.-D. proposed the concept. H.-S., C.P.-L. and M.-D. directed the research. C.-T. and C.-L. completed most of the experiments. Z.-Y. contributed to the X-ray absorption fine structure spectroscopy and DFT calculations. X.-F., R.-H., Y.-L. and J.-C. conducted the synthesis and characterization of partial catalysts. Z.-Z. assisted with the structural characterizations of catalysts. H.-S., Z.-Y. and M.-D. co-wrote the manuscript. All authors participated in data analysis and manuscript discussion.

Competing interests

The authors declare no competing interests.

Additional information

Supplementary information The online version contains supplementary material available at https://doi.org/10.1038/s41467-022-31561-4.

Correspondence and requests for materials should be addressed to Cheng-Peng Li or Miao Du.

Peer review information *Nature Communications* thanks the anonymous reviewers for their contribution to the peer review of this work. Peer reviewer reports are available.

Reprints and permission information is available at http://www.nature.com/reprints

Publisher's note Springer Nature remains neutral with regard to jurisdictional claims in published maps and institutional affiliations.